e-Prime - Advances in Electrical Engineering, Electronics and Energy 1 (2021) 100001

Contents lists available at ScienceDirect

e-Prime - Advances in Electrical Engineering, Electronics and Energy

journal homepage: www.elsevier.com/locate/prime

Modeling of vanadium redox flow battery and electrode optimization with different flow fields

Qijiao He[a], Jie Yu[a], Zixiao Guo[b], Jing Sun[b], Siyuan Zhao[a], Tianshou Zhao[b,*], Meng Ni[a,*]

[a] Department of Building and Real Estate, Research Institute for Sustainable Urban Development (RISUD) & Research Institute for Smart Energy (RISE), The Hong Kong Polytechnic University, Hung Hom, Kowloon, Hong Kong, China
[b] Department of Mechanical and Aerospace Engineering, The Hong Kong University of Science and Technology, Clear Water Bay, Kowloon, Hong Kong, China

ARTICLE INFO

Keywords:
Vanadium redox flow battery
Numerical simulation
Electrode design
Concentration loss

ABSTRACT

The fibrous electrode is an essential component of the redox flow batteries, as the electrode structure influences the reactant/product local concentration, electrochemical reaction kinetics, and the pressure loss of the battery. A three-dimensional numerical model of vanadium redox flow battery (VRFB) was developed in this work. After model validation, simulations were conducted to understand the effects of electrode structural parameters on the battery performance. The gradient electrode design, specific surface area, porosity, and different flow fields were studied and optimized. The results show that in the large-size VRFB system, ensuring a large porosity can minimize the concentration polarization, which not only improves the battery performance, and also reduce the pressure loss. To further improve the mass transfer, fibers with larger diameter can be used, and the specific surface area of the electrode can be increased by modifying the surface of the fiber. The battery performance can be significantly improved with increasing specific surface area when the specific surface area is lower than 500,000. However, with further increase in specific surface area, the voltage of the battery remains almost constant at about 1.37 V. Its influence on interdigitated flow channel case is mainly in reducing pressure loss, and on serpentine flow channel case is directly reflected in improving battery performance.

1. Introduction

The increasingly more and more serious energy crisis and environmental problems has accelerated research activities on clean energy technologies worldwide [1–3]. Renewable solar and wind power are expected to play a key role for a sustainable society but they are intermittent and fluctuating, requiring effective energy storage for their wide applications. The aqueous flow battery system is promising for industrial applications, due to its fast response, high safety, and long life [4]. After discharge, the electrolyte of flow battery can be recharged using excess renewable power such as wind and solar. Then the chemical energy of the charged electrolyte can be converted back to electricity via the flow battery through discharge when the renewable power is insufficient. Thus, the capacity and power of the system can be decoupled and designed in various sizes. Compared with conventional hydrogen storage systems, liquid electrolytes are as easy and safe to transport and store as gasoline. The aqueous flow battery system is efficient, scalable, safe, able to operate continuously for a long time, and independent of the site [5,6].

Although aqueous flow battery system has been widely recognized as a promising candidate as large-scale energy storage systems for renewable energies [7–9], its widespread commercialization has been limited by the high cost. In addition to the development of new energy materials, the cost reduction can also rely on engineering design to improve performance. On the one hand, if the power density of the system can be increased, the size of the stack can be reduced, which means the number of stack components, such as membranes, electrodes, and bipolar plates can be reduced [10–12]. On the other hand, the volume of the electrolyte can be reduced by improving the electrolyte utilization efficiency. To improve the performance of the flow battery, activation losses related to the kinetics of vanadium redox reactions, ohmic losses related to electron and ion transport resistance, and the concentration losses related to mass transport of active species all need to be minimized. The reduction of these polarization losses depends on not only the improvement of materials but also the optimization of the structural design of cell components [13–16].

The all-vanadium redox flow battery (VRFB) shows great potential for large energy storage capacity and power output. Other kinds of aqueous flow battery systems have also received considerable focus. The zinc-bromine flow battery is first introduced by Lim et al. [17] which is another attractive energy storage system due to its simple chemical reactions, high energy density, excellent electrochemical reversibility,

---

* Corresponding authors.
E-mail addresses: metzhao@ust.hk (T. Zhao), meng.ni@polyu.edu.hk (M. Ni).

https://doi.org/10.1016/j.prime.2021.100001
Received 21 August 2021; Accepted 6 October 2021

and inexpensive reactant materials. Another flow battery that has received numerous studies is the soluble lead–acid flow battery (SLFB), which improves the all-round performance while reducing the capital costs based on the former the flow battery system. The SLFB concept was introduced by Pletcher et al. [18] which was designed as a viable option for large-scale energy storage applications. However, lead-acid batteries contain toxic materials. Inappropriate disposal of SLFB can poison the soil and water. Rechargeable zinc-air flow batteries are cheap, non-toxic, and have a compact system design. Bockelmann et al. [19] built a rechargeable zinc-oxygen flow battery that reached a peak power density of 270 mW cm^{-2} and a maximum current density of up to 600 mA cm^{-2}.

The performance and reliability of aqueous flow battery systems usually depend on key components design and operating variables. Lots of works have been done for the structural design optimization of flow batteries. The electrode is a crucial component to determine the battery performance. Mayrhuber et al. [20] developed laser-perforated carbon paper electrodes to enhance the accessibility of electrolytes and improve battery performances. S. Kumar et al. [21] investigated efficiencies and pressure drop of a VRFB with interdigitated flow field and serpentine flow field. The battery with a serpentine flow field achieved high energy efficiency and low pressure drop. Ionic-conducting membrane or separator is usually needed to avoid the crossover of electroactive species, which influence the voltage and coulombic efficiencies of flow batteries. The electrolyte influence the electrochemical performance notably, as its concentration and volume determined the energy capacity of the flow battery directly. Dassisti et al. [22] assessed the feasibility, effectiveness, and sustainability of three different methods for the synthesis of vanadium-based mixed-acid electrolytes. Topology optimization was applied by Yaji et al. [23,24] in recent years, which provided more approaches for the flow fields design and improved the battery performance. Yaji et al. [23] formulated flow fields design as a maximization problem for the generation rate of the vanadium species, incorporated typical porous model and introduced mass transfer coefficient coupled local velocity to study the dependencies of the topology optimized design with the porosity and pressure loss. Chen et al. [24] presented computational design based on topology optimization to automatically generate optimized 3D flow field design of VRFB to gain higher performance. Both papers found that interdigitated flow field is an optimal flow field. The operating conditions are also essential for flow batteries performance, such as the temperature and flow rate [25,26]. Ma et al. [25] found that with increasing flow rate, the capacity of the battery increases, but the system efficiency decreases and strategies were applied to optimize the system. Zhang et al. [26] found that with the increased operating temperature, the peak discharge power density increased but the capacity decays and coulombic efficiency dropped.

Electrodes are essential contributors to all voltage losses and key components to the flow battery performance. Kim et al. [27] designed activity gradient carbon felt in-plane direction, which can uniform of the reaction rates, enhance electrolyte utilization, and improve energy efficiency. The optimization works were based on flow-through batteries without considering the flow field effect. With flow field adopted, the battery can use thinner electrode to get lower ohmic loss and improve cell performance including limiting current density and peak power density. Meanwhile, the numerical simulation is very essential to optimize the flow battery design.While the numerical studies on flow-by batteries are more based on single-channel and 2D models without considering the influence of rib, the in-plane variable changes, and concentration loss [28,29]. Jiang et al. [28] designed gradient porous electrode in through-plane direction and founded the design can uniform the local reaction current density and increase capacity. Tsushima et al. [29] established a 2D model to study the influence of electrode properties and channel geometry on battery performance and conducted multiple-parameter optimization for improving the design of VRFB. To further understand the coupling effects of flow field and electrode structure on battery performance under wider operating conditions, the 3D model is developed to improve the flow battery performance by optimizing the electrode microstructure in this paper. New structures are numerically designed to optimize electrodes of the VRFB. At the present stage, due to the use of graphite felt as the electrode material, Darcy's law is adopted for simulation, isotropy is assumed, and permeability coefficient is set as constant which does not change with space. For new electrode structures design, such as gradient electrodes, the flow in electrodes should be considered as anisotropic and the permeability coefficient should vary with the spatial position.

2. Mathematical model

A computational model is built to evaluate the electrode structural design for improving the battery performance. To reduce the computational cost without losing accuracy, half-cell computational domain is adopted in this study. The half-cell computational domain composes a flow field and an electrode for the positive/negative side, as shown in Fig. 1.

The reactions occurring in electrodes of vanadium redox flow batteries (VRFB) can be expressed as:

At positive electrode: $VO^{2+} + H_2O - e^- \underset{disch\arg e}{\overset{ch\arg e}{\rightleftharpoons}} VO_2^+ + 2H^+$

At negative electrode: $V^{3+} + e^- \underset{Disch\arg e}{\overset{Ch\arg e}{\rightleftharpoons}} V^{2+}$

With the assumption that the second step of H_2SO_4 dissociation is ignored, the electrolyte comprises 1 M vanadium ions and 4 M HSO_4^-. The inlet species concentration is determined by electrolyte SOC:

$$\frac{c_{V^{2+}}}{c^0_{V_{total}}} = \frac{c_{VO^{2+}}}{c^0_{V_{total}}} = SOC$$

$$\frac{c_{V^{3+}}}{c^0_{V_{total}}} = \frac{c_{VO^{2+}}}{c^0_{V_{total}}} = (1 - SOC)$$

where $c^0_{V_{total}}$ is initial total vanadium ion concentration and is set to 1 M.

The assumptions and simplifications used in the present work are as follows:

1. The transient model is simplified as a stationary model, considering that the reservoir is sufficiently large.
2. The entire domain is assumed to be isothermal.
3. The fluid flow is treated as incompressible.
4. The possible side reactions such as oxygen and hydrogen evolutions are neglected.

The mass and the momentum conservation for electrolyte in both the channel and porous electrode can be expressed with the Navier-Stokes equation and Brinkman equation respectively:

$$\rho \nabla \cdot \vec{u} = 0 \tag{1}$$

$$\rho(\vec{u} \cdot \nabla)\vec{u} = -\nabla p + \nabla \cdot \left[\mu\left(\nabla\vec{u} + (\nabla\vec{u})^T\right)\right] \tag{2}$$

$$\frac{\rho}{\varepsilon^2}(\vec{u} \cdot \nabla)\vec{u} = -\nabla p + \nabla \cdot \left[\frac{\mu}{\varepsilon}\left(\nabla\vec{u} + (\nabla\vec{u})^T\right)\right] - \frac{\mu}{k}\vec{u} \tag{3}$$

where ε is the porosity of the porous electrode, p is the pressure, μ is the dynamic viscosity of the fluid and k is the permeability of the porous electrode.

The specific surface area of the electrode, a, was determined by fiber diameter and porosity, which can be calculated by [30]:

$$a = \frac{4(1 - \varepsilon)}{d_f} \tag{4}$$

where d_f is the fiber diameter. The permeability of the porous electrode is expressed as [31]:

$$k = \frac{d_f^2 \varepsilon^3}{16 k_{ck}(1 - \varepsilon)^2} \tag{5}$$

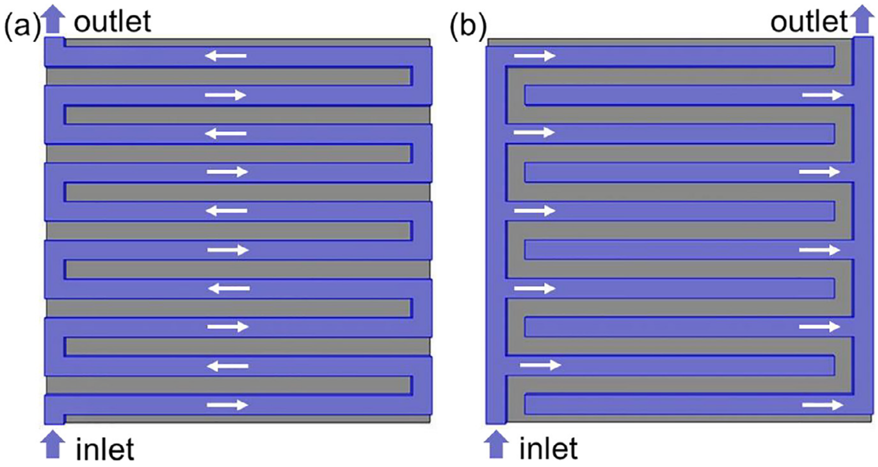

Fig. 1. Half-cell computational domain of VRFB, serpentine flow channel (a), and interdigitated flow channel (b).

where k_{ck} is the dimensionless Carman-Kozeny constant which depends on the shape and orientation of the fibrous material.

Nernst-Plank equation [32] is employed to describe the transport of dilute species in the porous electrode which comprises diffusive, migrative, and convective items:

$$\vec{N}_i = -D_i^{eff} \nabla c_i - \frac{z_i c_i D_i^{eff}}{RT} F \nabla \phi_e + \vec{u} c_i \tag{6}$$

$$\nabla \cdot \vec{N}_i = S_i \tag{7}$$

where the index i represents the species, and N_i is the flux of the species. S_i is the species molar source term, which represents the generation rate of species due to the electrochemical reactions. c_i and z_i are molar concentration and charge number of species i, respectively. R is the ideal gas constant, T is temperature, and F is Faraday's constant. ϕ_e is the potential in the electrolyte. The dissociation of $HSO_4{}^-$ is neglected in this simulation.

The effective diffusivity D_i^{eff} is corrected according to the Bruggeman correction [33]:

$$D_i^{eff} = \varepsilon^{1.5} D_i \tag{8}$$

Charge transport in the electrode for negative and positive sides is solved as:

$$\nabla \cdot \vec{i}_s = -\sigma_s^{eff} \nabla^2 \phi_s = i_{neg} \tag{9}$$

$$\nabla \cdot \vec{i}_e = -\sigma_e^{eff} \nabla^2 \phi_e = i_{neg} \tag{10}$$

where $\vec{i}_s$ is the current density in the electrode, $\vec{i}_e$ is the current density in the electrolyte. σ^{eff} and ϕ are the effective electric conductivity and potential. The positive electrode has similar equations for charge transport. The electrochemical reactions occurring on the surfaces of solid fiber in the electrode can be expressed by the Butler-Volmer equation [32]:

$$i_{neg} = aFk_{0,neg} c_{V^{2+}}^{\alpha_{c,neg}} c_{V^{3+}}^{\alpha_{a,neg}} \left[\frac{c_{V^{3+}}^s}{c_{V^{3+}}} \exp\left(-\frac{\alpha_{c,neg} F \eta_{\mathrm{neg}}}{RT} \right) - \frac{c_{V^{2+}}^s}{c_{V^{2+}}} \exp\left(\frac{\alpha_{a,neg} F \eta_{neg}}{RT} \right) \right] \tag{11}$$

$$i_{\mathrm{pos}} = aFk_{0,pos} c_{VO^{2+}}^{\alpha_{c,pos}} c_{VO_2{}^+}^{\alpha_{a,pos}} \left[\frac{c_{VO_2{}^+}^s}{c_{VO_2{}^+}} \exp\left(-\frac{\alpha_{c,pos} F \eta_{pos}}{RT} \right) - \frac{c_{VO^{2+}}^s}{c_{VO^{2+}}} \exp\left(\frac{\alpha_{a,pos} F \eta_{pos}}{RT} \right) \right] \tag{12}$$

where $k_{0,\mathrm{neg}}$ and $k_{0,\mathrm{pos}}$ is the reaction constant of the reactions occurring in negative and positive sides, respectively, $\alpha_{a,neg}$ and $\alpha_{c,neg}$ are anodic and cathodic charge transfer coefficient of negative half-reaction, $\alpha_{a,pos}$ and $\alpha_{c,pos}$ are anodic and cathodic charge transfer coefficient of positive half-reaction.

Overpotentials are defined as follows:

$$\eta_{\mathrm{neg}} = \phi_{s,neg} - \phi_{e,neg} - E_{eq,neg} \tag{13}$$

$$\eta_{pos} = \phi_{s,pos} - \phi_{e,pos} - E_{eq,pos} \tag{14}$$

Equilibrium potentials are calculated via:

$$E_{eq,\mathrm{neg}} = E_{neg}^0 + \frac{RT}{F} \ln\left(\frac{c_{V^{3+}}}{c_{V^{2+}}} \right) \tag{15}$$

$$E_{eq,\mathrm{pos}} = E_{pos}^0 + \frac{RT}{F} \ln\left(\frac{c_{VO_2^+} c_{H^+}^2}{c_{VO^{2+}}} \right) \tag{16}$$

where E_{neg}^0 and E_{pos}^0 are equilibrium potentials at the standard condition.

The vanadium ions concentration at the surface of carbon fibers can be calculated by balancing the generation rate of reactants and the rate of transfer from the bulk to the interface. A quasi-equilibrium state assumption is adopted for the ions transport considering that SOC of electrolyte changes slowly due to relatively small volume of electrolyte in the cell compared with that in the reservoirs. Concentrations of VO^{2+} and $VO_2{}^+$ at the surface are derived as:

$$\mathrm{c}_{VO^{2+}}^s = \frac{B_1 c_{VO_2^+} + (1 + B_1) c_{VO^{2+}}}{1 + A_1 + B_1} \tag{17}$$

$$\mathrm{c}_{VO_2^+}^s = \frac{A_1 c_{VO^{2+}} + (1 + A_1) c_{VO_2^+}}{1 + A_1 + B_1} \tag{18}$$

where

$$A_1 = \frac{k_{0,pos}}{k_m} c_{VO^{2+}}^{\alpha_{c,pos}-1} c_{VO_2^+}^{\alpha_{a.pos}} \exp(\alpha_{a,pos} F \eta_{pos}) \tag{19}$$

$$B_1 = \frac{k_{0,pos}}{k_m} c_{VO^{2+}}^{\alpha_{c,pos}} c_{VO_2^+}^{\alpha_{a,pos}-1} \exp(-\alpha_{c,pos} F \eta_{pos}) \tag{20}$$

Concentrations of V^{2+} and V^{3+} at the surface are derived as:

$$\mathrm{c}_{V^{2+}}^s = \frac{B_2 c_{V^{3+}} + (1 + B_2) c_{V^{2+}}}{1 + A_2 + B_2} \tag{21}$$

$$\mathrm{c}_{V^{3+}}^s = \frac{A_2 c_{V^{2+}} + (1 + A_2) c_{V^{3+}}}{1 + A_2 + B_2} \tag{22}$$

where

$$A_2 = \frac{k_{0,neg}}{k_m} c_{V^{2+}}^{\alpha_{c,neg}-1} c_{V^{3+}}^{\alpha_{a,neg}} \exp(\alpha_{a,neg} F \eta_{neg}) \tag{23}$$

Table 1
Electrochemical parameters and electrode properties.

Parameters	Symbols (Unit)	Value
a	Specific surface area (m^{-1})	various
d_f	Carbon electrode fiber (μm)	various
k_{ck}	Carman-Kozeny constant	4.28 [35]
σ_s	Electrode conductivity (S m^{-1})	200
$k_{0,neg}$	The standard reaction rate constant of the negative side (m s^{-1})	6.8×10^{-7} [36]
$\alpha_{a,neg}$	Anodic charge transfer coefficient for the negative side	0.5
$\alpha_{c,neg}$	Cathodic charge transfer coefficient for the negative side	0.5
$k_{0,pos}$	The standard reaction rate constant of the positive side (m s^{-1})	1.7×10^{-7} [37]
$\alpha_{a,pos}$	Anodic charge transfer coefficient for the positive side	0.5
$\alpha_{c,pos}$	Cathodic charge transfer coefficient for the positive side	0.5
E^0_{neg}	Standard potential (negative) (V)	−0.225 [38]
E^0_{pos}	Standard potential (positive) (V)	1.004 [38]

Table 2
Electrolyte properties.

Parameters	Symbols (Unit)	Value
ρ	Electrolyte density (kg m^{-3})	1.45×10^3
μ	Electrolyte viscosity (Pa•s)	4.93×10^{-3} [39]
D_H	Proton diffusion coefficient (m^2 s^{-1})	9.31×10^{-9} [32]
D_{HSO4}	HSO_4 diffusion coefficient (m^2 s^{-1})	1.33×10^{-9} [32]
D_{VII}	V(II) diffusion coefficient in the electrolyte (m^2 s^{-1})	2.40×10^{-10} [37]
D_{VIII}	V(III)diffusion coefficient in the electrolyte (m^2 s^{-1})	2.40×10^{-10} [37]
D_{IV}	V(IV)diffusion coefficient in the electrolyte (m^2 s^{-1})	3.90×10^{-10} [37]
D_V	V(V)diffusion coefficient in the electrolyte (m^2 s^{-1})	3.90×10^{-10} [37]

Table 3
Operating and geometric parameters.

Parameters	Symbols (Unit)	Value
C-,H0	Initial $H+$ concentration in negative side (mol $m - 3$)	2500
$C_{-,HSO4^\circ}$	Initial HSO_4^- concentration in negative side (mol m^{-3})	4000
$C_{II}{}^0$	Initial V(II) concentration (mol m^{-3})	500
$C_{III}{}^0$	Initial V(III) concentration (mol m^{-3})	500
T	Operating temperature (K)	298.15
ε_0	Uncompressed electrode porosity	0.94
ε	Compressed electrode porosity	various
h	Channel depth (mm)	1.5
w	Channel width (mm)	1

$$B_2 = \frac{k_{0,neg}}{k_m} c_{V^{2+}}^{\alpha_{c,neg}} c_{V^{3+}}^{\alpha_{a,neg}-1} \exp(-\alpha_{c,neg} F \eta_{neg}) \tag{24}$$

The local mass transfer coefficient can be calculated approximately [34]:

$$k_m = 1.6 \times 10^{-4} |\vec{u}|^{0.4} \tag{25}$$

At the outlet of the channel, the pressure is set to be zero as the reference and concentration gradient is assumed to be zero. Zero potential was adopted at the contact of the porous electrode and the current collector. Various currents were applied at the interface between electrode and membrane uniformly under different work conditions. This condition is more suitable for small scale batteries but may become less accurate when the size of the battery is sufficiently large. All the other boundaries were impermeable to the mass, electron, and species transfer. The parameters of geometry, material properties, and operating conditions were listed in Tables 1–3.

The above equations were solved based on the finite-element method within COMSOL MULTIPHYSICS. The fluid flow in channels and electrodes was described by the Free and Porous Media Flow option. The mass transport coupled with electrochemical reactions was described by the Second Current Distribution and the Transport of Diluted Species options. The number of 652,915 was chosen for the degrees of freedom in the subsequent simulations, based on the mesh independence check as shown in Fig. 2(a). The relative tolerance was set to 1×10^{-6}.

To validate the proposed model in this work, both the polarization curve and charge-discharge curves of simulation results are compared with those of experiments under different operating conditions. As flow rate can be easily controlled in battery testing, the simulations are conducted at given flow rates. For the polarization curve case, two pieces of the commercially available carbon paper (280 μm, SGL, 39 AA) were compressed with the total thickness of 0.5 mm as electrode. The active area of the electrode is 2 cm × 2 cm, and the inlet volume flow rate is 20 ml/min. In the charge-discharge curves, the commercially available graphite felt (GFA 6 EA, porosity 0.95) with an active area of 3 cm × 3 cm and a thickness after compression of 0.8 mm were used as positive and negative electrodes. The inlet volume flow rate is 45 ml/min. The height of the channel is 1.5 mm, the width of both the channel and rib is 1 mm in both cases. The cell voltage measured in experiments is time-dependent, which needs to be transferred into the function of SOC as simulation results. The initial SOC of both the charge and discharge process is determined with OCV, and the change in SOC is captured with the capacity variance measured in experiments. As depicted in Fig. 2(b) and (c), the simulation results show good agreement with experimental data in a relatively wide range of current density and SOC. The discrepancies can be ascribed to the reaction rate constant and mass transfer coefficient applied. The rapid change of vanadium species, which dissatisfies the quasi-steady conditions of mass transport and electrochemical reactions at the surface of carbon fibers. The slight discrepancies also may result from the estimated properties of the electrode and ion crossover. In the following parametric simulation study, the height of the channel is set as 1.5 mm, the width of both the channel and rib is set as 1 mm. The thickness of electrode is set as 0.5 mm and the active area of the electrode is set as 2 cm × 2 cm for both the serpentine and interdigitated flow field cases.

3. Results and discussion

3.1. Effect of gradient electrode design

In the flow battery, ensuring good mass transport is essential for the electrolytes transport from the flow field side to the membrane side. Thus, the electrode of the flow field side is supposed to have sufficiently

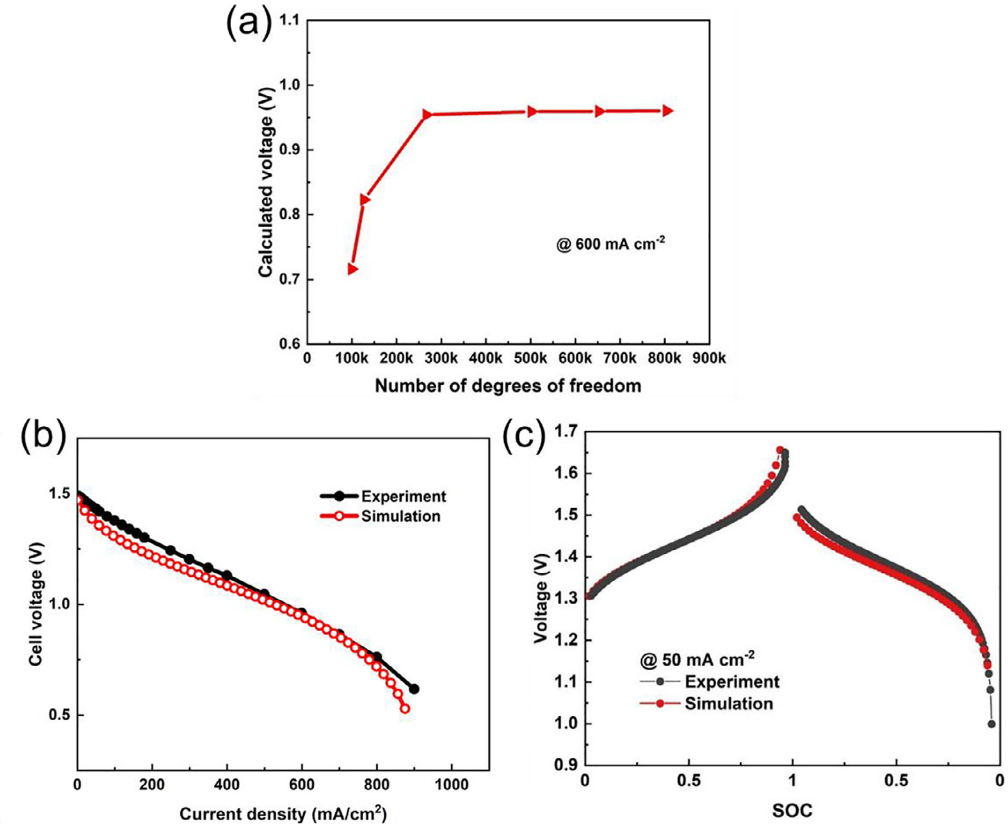

Fig. 2. Mesh independence (a) and model validation (b) and (c).

high porosity. If the porosity is too small, the electrode utilization is very low, especially in the region close to the membrane, which can increase the polarization and decrease the performance of the battery. High porosity can cause the main reaction region to occur on the membrane side with enough reactants and lower ionic conductivity. Enough surface area should be set near the membrane side to enhance the redox reactions, which can decrease the activation loss effectively. Based on this, the gradient electrode design in the z-direction with serpentine flow field is applied, the schematic of which is shown in Fig. 3(a). The electrode has a gradient pore structure with the porosity gradually increasing from the membrane side to the flow field-side while the reaction surface area gradually increasing from the flow field side to the membrane side. This design can avoid the loss of active surface area at the main reaction region and enhance the transport properties of the electrode simultaneously. Although, from the discharge curves in Fig. 3(b), it is not obvious that the gradient electrode can improve the battery performance. But it can still be seen in Fig. 3(c) that the current density distribution shows the comparison of electrochemical reaction area and intensity to verify the rationality of the design. When the electrode porosity is 0.8, the electrochemical reaction mainly occurs at the flow field side due to the high resistance for mass transport, which leads to uneven current density distribution in **Fig. 3(c)**. When the electrode porosity is 0.95, sufficient electrolyte can be transported to the membrane side, the membrane side becomes the main area that occurs electrochemical reaction. However, the high porosity can cause low specific surface area, which further increases the polarization overpotential. For comparison, the gradient electrode porosity design leads to a more uniform distribution of current density along the through-plane direction. The gradient design can balance transport properties and active surface areas at the same time, which can decrease the high-overpotential in the through-plane direction.

The uniformity of reactants in the battery is also an essential index affecting the battery performance. Along the direction from the inlet to outlet, the overpotential variates from concentration difference due to the abundant reactants at the inlet and depleted reactants at the outlet. Based on this, the gradient electrode strategies can be applied to the battery for better performance.

To use the electrode active area of the VRFB efficiently, the lower porosity was set on the inlet side and the higher porosity was set to the outlet side in the y-direction as shown in Fig. 4((a), and lower porosity was set on the inlet and outlet side and the higher porosity was set to the other side in the x-direction as shown in Fig. 5(a). The setting can promote the reaction performance where the reactant concentration is depleted. Although, from the discharge curves in Fig. 4(b) and Fig. 5(b), it is also not obvious that the gradient electrode can improve the battery performance. But it can still be seen in Fig. 4(c) and Fig. 5(c) that the current density distribution shows the comparison of electrochemical reaction area and intensity to verify the rationality of the design. When the porosity of the electrode is 0.8, the electrochemical reactions in the whole are lower due to the poor mass transport. When the porosity of the electrode is 0.95, good mass transport helps electrochemical reactions take place in the whole cell.

The current distribution results of the gradient electrode are in between the results of two uniform porosity, and these results indicate that the influence of concentration polarization is significant in the in-plane direction. At the in-plane, activated polarization is no longer the main factor affecting the performance of the battery. In the case of no need to ensure a large reaction area, it should be given priority to improve the porosity to ensure enough transfer of reactants and reduce the concentration polarization to improve the performance of the battery.

In addition to the impact on battery performance, large porosity and gradient electrode design can reduce the pump power consumption required to provide electrolyte flow by reducing pressure drop as shown in Fig. 6. The influence of pump power consumption on the overall efficiency of the system should be considered in the following electrode optimization.

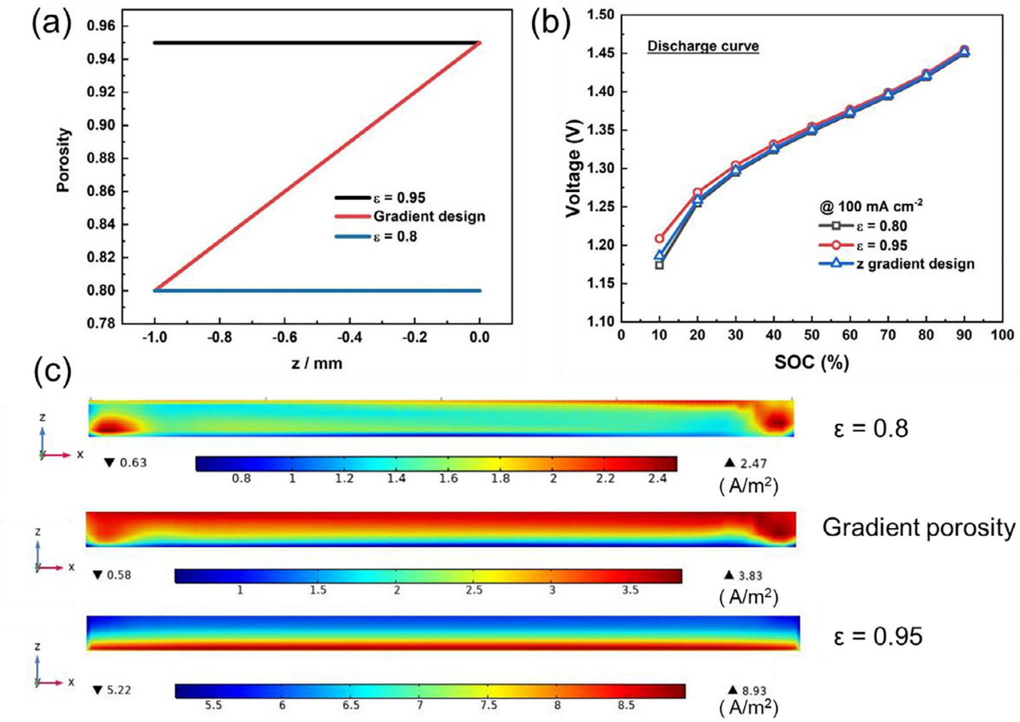

Fig. 3. The distributions of porosity (a), the simulated discharge curves (b), and local current density distributions (c) of VRFBs with different electrode porosity design strategies in the z-direction.

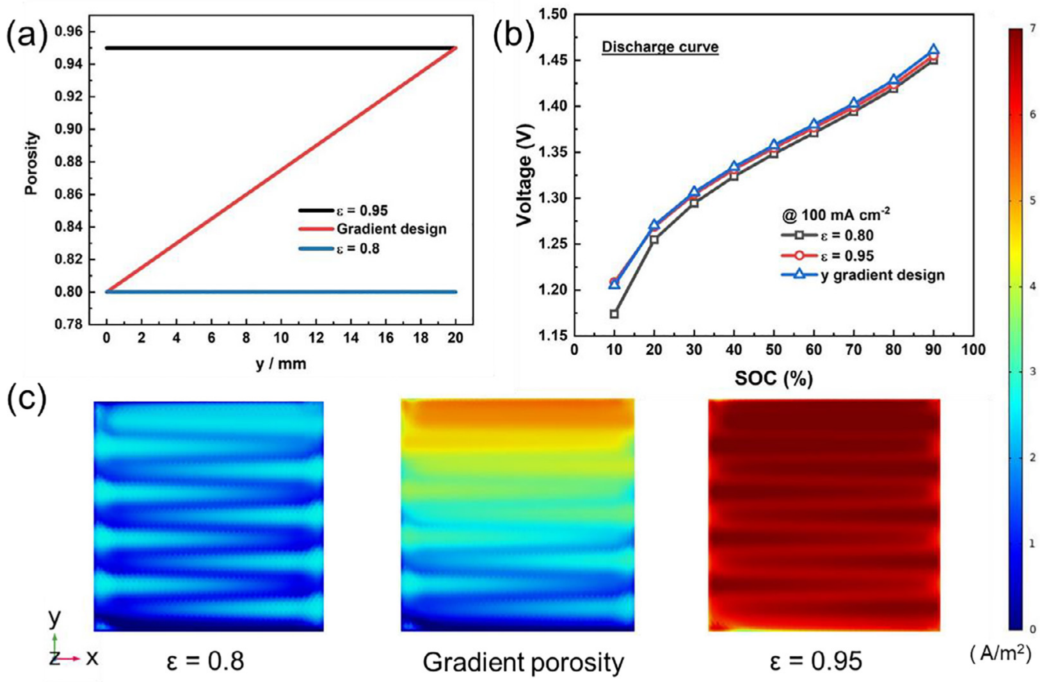

Fig. 4. The distributions of porosity (a), the simulated discharge curves (b) and local current density distributions (c) of VRFBs with different electrode porosity design strategies in the y-direction.

In previous results, the inlet volume flow rate was set as 45 ml/min to be consistent with the lab-scale cell experiment setting. But in the industry-scale stack, the average flow rate per cm^2 is different. For example, the flow rate of a lab-scale high-performance small battery with 4 cm^2 active area of the electrode is operated at a flow rate of 45 m L/min, and the average flow rate/cm^2 is larger than 11.25 mL/(min•cm^2). The flow rate of a 1 kW stack, which contains 8 cells, has a 400 cm^2 active area of the electrode and is operated at a flow rate of 5–6 L/min, the average flow rate/cm^2 of it is only 1.5–1.8 mL/(min•cm^2). To study the battery performance at a low flow rate, we convert the flow rate from the stack to a small battery as 6 ml/min, and the results are shown in Fig. 7 and Fig. 8. These results reinforce the previous points. At the low flow rate, concentration polarization dominates the performance of the battery. All designs should ensure high mass transfer at first. In our re-

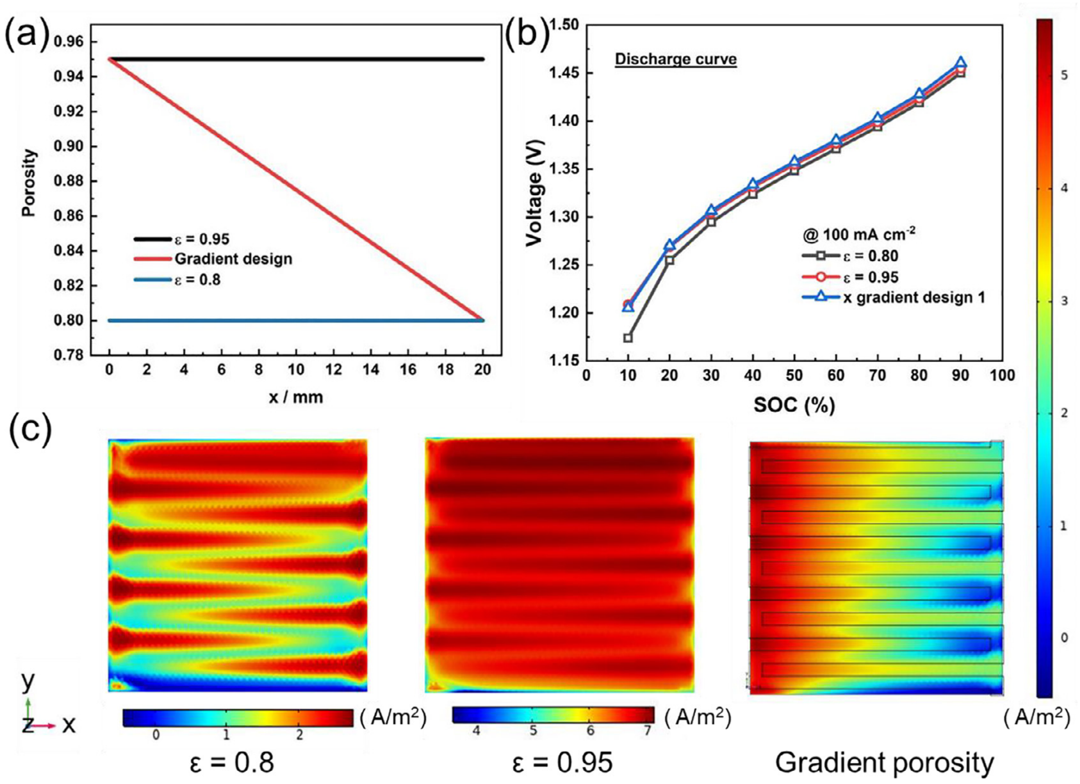

Fig. 5. The distributions of porosity (a), the simulated discharge curves (b), and local current density distributions (c) of VRFBs with different electrode porosity design strategies in the x-direction.

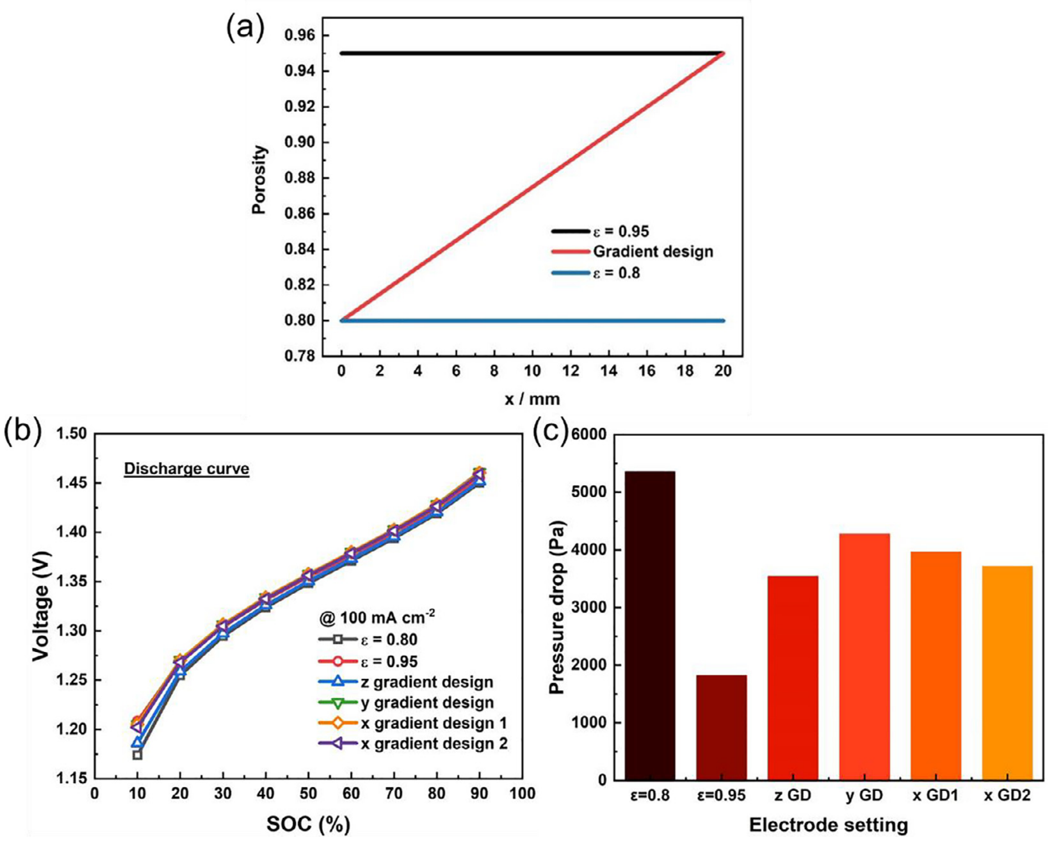

Fig. 6. The distributions of porosity (a), the simulated discharge curves (b), and pressure drop (c) of VRFBs with different electrode porosity design strategies.

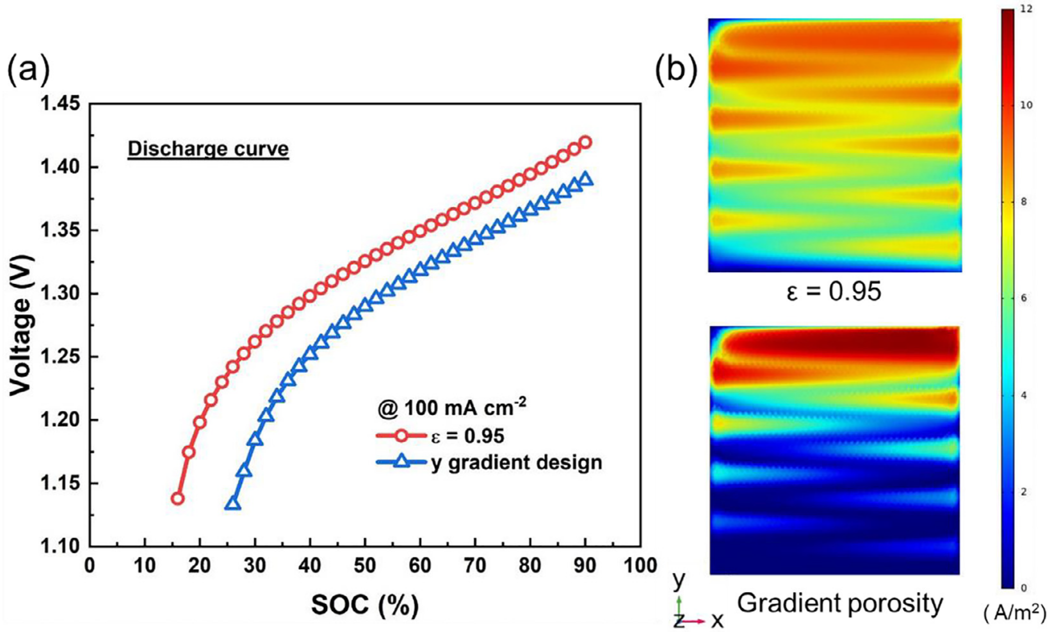

Fig. 7. The discharge curves (a) and current density distributions (b) of VRFBs with different electrode porosity design strategies in the y-direction at a low inlet flow rate.

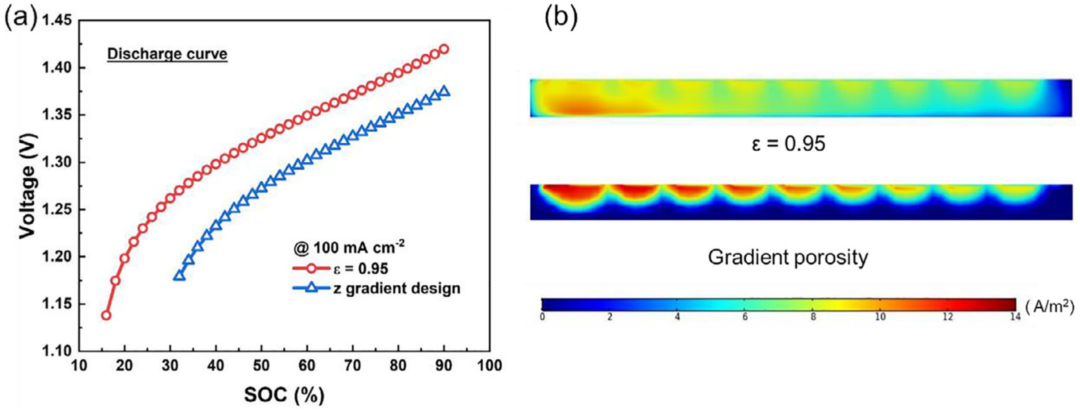

Fig. 8. The discharge curves (a) and current density distributions (b) of VRFBs with different electrode porosity design strategies in the z-direction at a low inlet flow rate.

sults, we can also find that due to the forced convection under the ribs, the increased velocity brought sufficient reactants, making the electrochemical reaction under the ribs more intense as shown in Fig. 7(b) and Fig. 8(b).

The gradient range was divided into different levels for parameter studies. The electrode thickness, the porosity gradient are coupled to find the influence.

3.2. Effect of porosity and specific surface area

The performance of the electrode mainly depends on the concentration overpotential caused by mass transfer and the activation overpotential caused by electrochemical reactions. Increasing the porosity improves the mass transfer to reach higher battery performance but decreases the specific surface area and tends to increase the activation loss. When the concentration overpotential limits the battery performance such as at a high current density, a high porosity is needed to enhance mass trasnfer. When the activation overpotential is the limiting factor, a lower porosity is needed to achieve high specific surface area and a low activation loss. The method of increasing the specific surface area in the experiment is based on the surface modification of electrode fibers in the electrospinning process, such as making nano-holes. Jing et at. [40] proposed a novel ZIF-8-assisted etching approach to form holey fibers, which allowed the formation of holey fibers with small pores of ~50 nm, offering large active surface areas for redox reactions.

As the results are shown in Fig. 9(a) and (b), we studied the relationship between the specific surface area and battery performance, the charge-discharge curves indicate that the performance of the battery increases rapidly when the specific surface area is less than 20,000 m^2/m^3. With a further increase in specific surface area (> 20,000 m^2/m^3), the battery performance becomes insignificant. In the present results, we found that porosity played a dominant role to influence the battery performance compared with specific surface area according to Fig. 9(c) under the investigated electrode thickness and operating condition.

Through the polarization curves in Fig. 10(a), we can better understand the main polarization of different porosity occurs at which current density range. At a high current density, the performance of the flow battery is limited by the mass transfer process, thus a higher porosity is beneficial for reducing the concentration overpotential and enhancing the battery performance (Fig. 10b). While at a low current density,

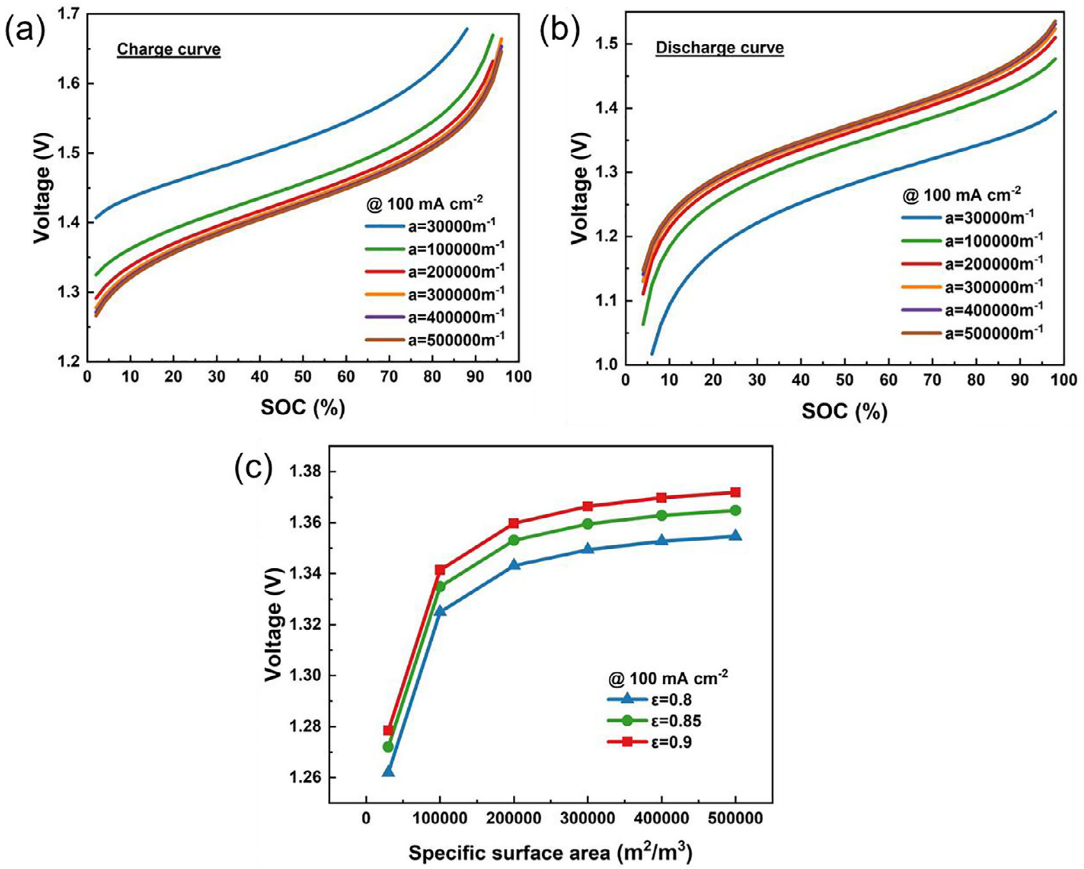

Fig. 9. The charge curves (a) and discharge curves (b) of different specific surface area and specific surface area-voltage relationships of different porosity (c).

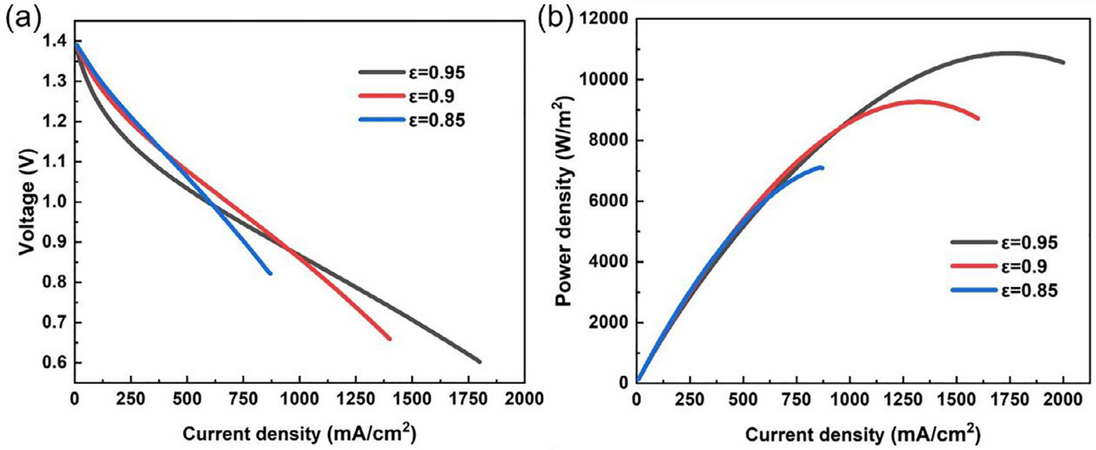

Fig. 10. The polarization curves (a) and current density-power density relationships (b) of different porosity.

the activation loss due to electrochemical reaction is more significant than the concentration loss. Thus, a lower porosity increases the specific surface areas, reduces the activation overpotential, and improves the battery performance.

3.3. Effect of fiber diameter and flow pattern

However, in the experiment, to minimize contact resistance and avoid electrolyte leakage, larger porosity is difficult to achieve after electrode assembly compression. Another way to increase permeability for good mass transfer is by electrospinning, which controls the electrode fiber diameter. When the electrode fiber diameter increasing, the permeability of the electrode is increasing, and the specific surface area is decreasing. Combined with the modification technology, the fiber diameter, and specific surface area both can be controlled. According to Fig. 11, after modification, the voltages achieved by the batteries with different fiber diameters at low current density coincide at a large specific surface area. Modifying larger fiber diameter electrodes can not only ensure high permeability but also decrease the active loss. The sensitive section is also obvious in Fig. 11. Finding the sensitive section can help to avoid excessive modification to ensure the mechanical strength of the fiber for long-term use.

We found that the sensitivity of VRFB with different flow patterns is also different with the changes of electrode fiber diameter. This is re-

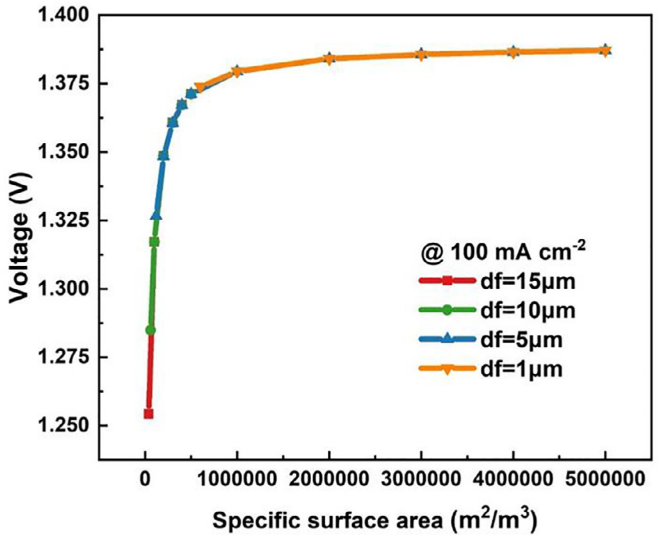

Fig. 11. The specific surface area-voltage relationships of different fiber diameters with the interdigitated flow channel.

Table 4
Fluid parameters with different flow patterns.

Flow patterns	d_f (μm)	△p (Pa)	$\bar{u}$ in electrode (m/s)
Interdigitated case	1	45,724	5.9294E-4
	10	623	5.9294E-4
Serpentine case	1	2180	2.1815E-6
	10	2003	3.4266E-4

lated to the mass transport way of the electrolyte in VRFB with different flow patterns. In Fig. 11, we could see that the battery performance of interdigitated flow channel VRFB only corresponds to the specific surface area, so we conduct the same calculation with the serpentine flow channel case, the results are shown in Fig. 12. Same as Fig. 11, there is no obvious battery performance increasing between different fiber diameter cases in interdigitated cases. But in the serpentine flow channel case, the battery performance increases a lot due to good mass transport with a larger fiber diameter setting. We also check the average electrolyte velocity in electrode and pressure drop between inlet and outlet of interdigitated and serpentine flow channel case, as shown in Table 4. The average electrolyte velocity of the serpentine case increases with fiber diameter increasing. Due to the forced convection, the pressure drop between the inlet and outlet of an interdigitated case decreases a lot with the fiber diameter increasing, which will also help improve the whole efficiency of the system by decreasing the pressure loss.

4. Conclusions

A numerical model has been developed to simulate the coupled transport and reaction processes in VRFB systems. The species transport, charge transport, fluid flow, and electrochemical reactions are fully considered.

New structures are numerically designed to optimize electrodes of the VRFB. In the previous study, isotropy is assumed, and the permeability coefficient is set as constant which does not change with space. For new gradient electrode structures design, the flow in electrodes is considered that anisotropic and the permeability coefficient can vary with the spatial position. For the newly designed electrode, surface (activity) and structure (macroscopic and microscopic) are balanced to get good reactivity, large reaction area and reactants can be transferred in

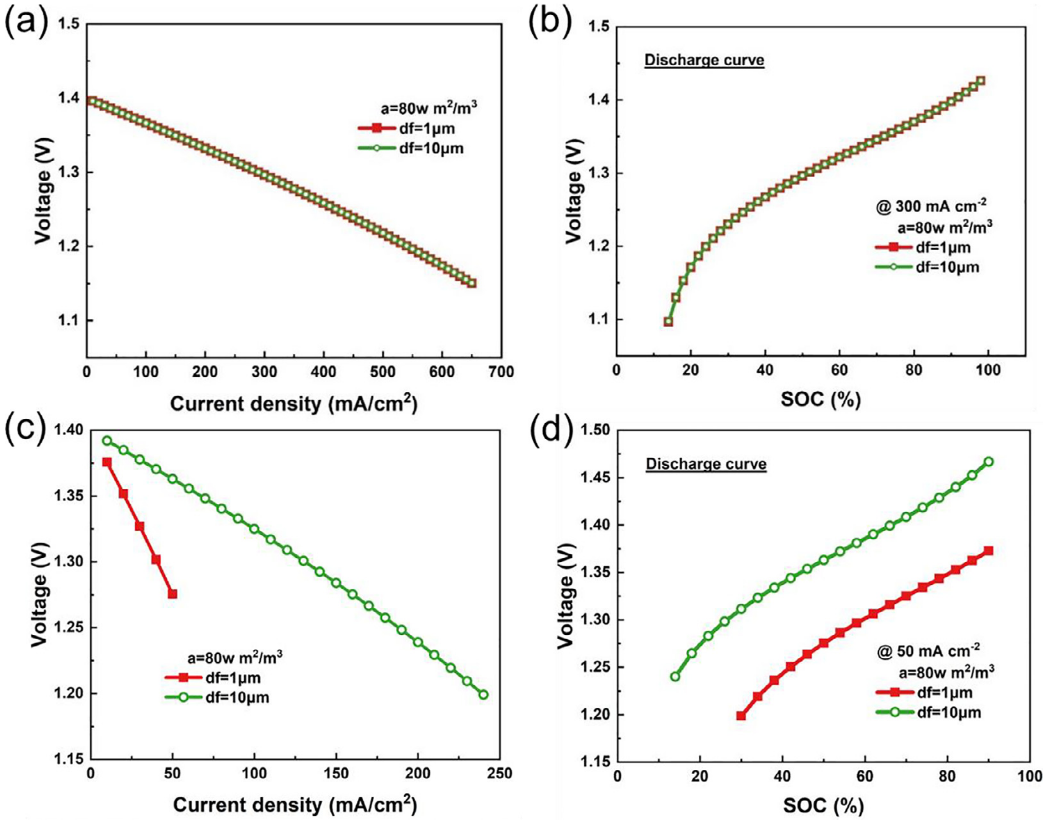

Fig. 12. The polarization (a) and discharge (b) curve of interdigitated flow channel VRFB and the polarization (c) and discharge (d) curve of serpentine flow channel VRFB with different fiber diameters setting.

time. By using porosity and fiber diameter as the controlling conditions of permeability, improved specific surface area was coupled to optimize the electrode design.

The optimization of the electrode is related to the flow pattern. For large-scale VRFB systems, the flow per unit area is much lower than that of small-scale VRFB systems. In this case, concentration polarization is the main loss, and the performance improvement obtained by improving the flow pattern design is more obvious. At a large scale, the optimization design of electrodes for the flow field with poor mass transfer effect is not effective. The principle is to increase the porosity as much as possible so that the reactants can be more uniformly distributed in the whole electrode. Meanwhile, It is found that the electrochemical reaction under the rib is stronger than under the channel because the forced convection of the under rib flow makes the electrolytes flow faster, bringing in the reactants faster and taking away the products in time. To ensure better mass transfer, in addition to the use of large porosity, fiber diameter can also be controlled to increase permeability. Although the mass transfer is improved, the specific surface area will decrease correspondingly, thus increasing the activation loss. To solve this problem, the fiber surface can be modified to obtain a larger specific surface area. The battery performance can be significantly improved with increasing specific surface area when the specific surface area is lower than 50,0000. However, with further increase in specific surface area, the voltage of the battery remains almost constant at about 1.37 V. Its influence on interdigitated flow channel case is mainly in reducing pressure loss, from 45,724 Pa to 623 Pa, and on serpentine flow channel case is directly reflected in improving battery performance by increasing the average velocity of electrode from 2.1815×10^{-6} m/s to 3.4266×10^{-4} m/s.

The built three-dimensional numerical toolkit can be further applied to conduct large-scale VRFB system optimization, including flow pattern optimization, electrodes optimization, and thermal management optimization.

Declaration of Competing Interest

The authors declare that they have no known competing financial interests or personal relationships that could have appeared to influence the work reported in this paper.

Acknowledgement

This research is supported by a grant under the Theme-based Scheme (project number: T23–601/17-R) from Research Grant Council, University Grants Committee, Hong Kong SAR.

References

[1] M. Ni, 2D thermal modeling of a solid oxide electrolyzer cell (SOEC) for syngas production by H_2O/CO_2 co-electrolysis, Int. J. Hydrogen Energy 37 (8) (2012) 6389–6399.

[2] M. Ni, M.K.H. Leung, D.Y.C. Leung, Energy and exergy analysis of hydrogen production by a proton exchange membrane (PEM) electrolyzer plant, Energy Convers. Manage. 49 (10) (2008) 2748–2756.

[3] P. Tan, M. Liu, Z. Shao, et al., Recent advances in perovskite oxides as electrode materials for nonaqueous lithium–oxygen batteries, Adv. Energy Mater. 7 (13) (2017) 1602674.

[4] H. Jiang, L. Wei, X. Fan, J. Xu, W. Shyy, T. Zhao, A novel energy storage system incorporating electrically rechargeable liquid fuels as the storage medium, Science Bulletin 64 (4) (2019) 270–280.

[5] H.R. Jiang, M.C. Wu, Y.X. Ren, W. Shyy, T.S. Zhao, Towards a uniform distribution of zinc in the negative electrode for zinc bromine flow batteries, Appl. Energy 213 (2018) 366–374.

[6] M.C. Wu, T.S. Zhao, L. Wei, H.R. Jiang, R.H. Zhang, Improved electrolyte for zinc-bromine flow batteries, J. Power Sources 384 (2018) 232–239.

[7] P. Leung, X. Li, C.P. De León, L. Berlouis, C.J. Low, F.C. Walsh, Progress in redox flow batteries, remaining challenges and their applications in energy storage, RSC Adv. 2 (27) (2012) 10125–10156.

[8] R.M. Wittman, M.L. Perry, T.N. Lambert, B.R. Chalamala, Y. Preger, Perspective—A materials perspective on the reliability and safety of grid-scale aqueous batteries, J. Electrochem. Soc. (2020).

[9] M. Skyllas-Kazacos, G. Kazacos, G. Poon, H. Verseema, Recent advances with UNSW vanadium-based redox flow batteries, Int. J. Energy Res. 34 (2) (2010) 182–189.

[10] J. Sun, H.R. Jiang, M.C. Wu, X.Z. Fan, C.Y.H. Chao, T.S. Zhao, Aligned hierarchical electrodes for high-performance aqueous redox flow battery, Appl. Energy 271 (2020) 115235.

[11] J. Sun, H.R. Jiang, M.C. Wu, X.Z. Fan, C.Y.H. Chao, T.S. Zhao, A novel electrode formed with electrospun nano-and micro-scale carbon fibers for aqueous redox flow batteries, J. Power Sources (2020) 228441.

[12] Z. He, G. Cheng, Y. Jiang, Y. Li, J. Zhu, W. Meng, … L. Wang, Novel 2D porous carbon nanosheet derived from biomass: ultrahigh porosity and excellent performances toward V2+/V3+ redox reaction for vanadium redox flow battery, Int. J. Hydrogen Energy 45 (7) (2020) 3959–3970.

[13] G.C. Sedenho, D. De Porcellinis, Y. Jing, E. Kerr, L.M. Mejia-Mendoza, Á. Vazquez–Mayagoitia, … M.J. Aziz, Effect of molecular structure of quinones and carbon electrode surfaces on the interfacial electron transfer process, ACS Appl. Energy Mater. 3 (2) (2020) 1933–1943.

[14] R.K. Gautam, A. Verma, Uniquely designed surface nanocracks for highly efficient and ultra-stable graphite felt electrode for vanadium redox flow battery, Mater. Chem. Phys. (2020) 123178.

[15] V.P. Nemani, K.C. Smith, Assignment of energy loss contributions in redox flow batteries using exergy destruction analysis, J. Power Sources 447 (2020) 227371.

[16] R.K. Gautam, M. Kapoor, A. Verma, Tactical surface modification of a 3D graphite felt as an electrode of vanadium redox flow batteries with enhanced electrolyte utilization and fast reaction kinetics, Energy Fuels 34 (4) (2020) 5060–5071.

[17] H.S. Lim, A.M. Lackner, R.C. Knechtli, Zinc-bromine secondary battery, J. Electrochem. Soc. 124 (8) (1977) 1154.

[18] D. Pletcher, R. Wills, A novel flow battery: a lead acid battery based on an electrolyte with soluble lead (II) Part II. Flow cell studies, PCCP 6 (8) (2004) 1779–1785.

[19] M. Bockelmann, U. Kunz, T. Turek, Electrically rechargeable zinc-oxygen flow battery with high power density, Electrochem. Commun. 69 (2016) 24–27.

[20] I. Mayrhuber, C.R. Dennison, V. Kalra, E.C. Kumbur, Laser-perforated carbon paper electrodes for improved mass-transport in high power density vanadium redox flow batteries, J. Power Sources 260 (2014) 251–258.

[21] S. Kumar, S. Jayanti, Effect of flow field on the performance of an all-vanadium redox flow battery, J. Power Sources 307 (2016) 782–787.

[22] M. Dassisti, G. Cozzolino, M. Chimienti, A. Rizzuti, P. Mastrorilli, P L'Abbate, Sustainability of vanadium redox-flow batteries: benchmarking electrolyte synthesis procedures, Int. J. Hydrogen Energy 41 (37) (2016) 16477–16488.

[23] K. Yaji, S. Yamasaki, S. Tsushima, T. Suzuki, K. Fujita, Topology optimization for the design of flow fields in a redox flow battery, Struct. Multidiscip. Optimiz. 57 (2) (2018) 535–546.

[24] C.H. Chen, K. Yaji, S. Yamasaki, S. Tsushima, K. Fujita, Computational design of flow fields for vanadium redox flow batteries via topology optimization, J. Energy Storage 26 (2019) 100990.

[25] X. Ma, H. Zhang, C. Sun, Y. Zou, T. Zhang, An optimal strategy of electrolyte flow rate for vanadium redox flow battery, J. Power Sources 203 (2012) 153–158.

[26] C. Zhang, T.S. Zhao, Q. Xu, L. An, G. Zhao, Effects of operating temperature on the performance of vanadium redox flow batteries, Appl. Energy 155 (2015) 349–353.

[27] Y. Kim, Y.Y. Choi, N. Yun, M. Yang, Y. Jeon, K.J. Kim, J.I. Choi, Activity gradient carbon felt electrodes for vanadium redox flow batteries, J. Power Sources 408 (2018) 128–135.

[28] H.R. Jiang, B.W. Zhang, J. Sun, X.Z. Fan, W. Shyy, T.S. Zhao, A gradient porous electrode with balanced transport properties and active surface areas for vanadium redox flow batteries, J. Power Sources 440 (2019) 227159.

[29] S. Tsushima, T. Suzuki, Modeling and simulation of vanadium redox flow battery with interdigitated flow Field for optimizing electrode architecture, J. Electrochem. Soc. 167 (2) (2020) 020553.

[30] R. Carta, S. Palmas, A.M. Polcaro, G. Tola, Behaviour of a carbon felt flow by electrodes Part I: mass transfer characteristics, J. Appl. Electrochem. 21 (9) (1991) 793–798.

[31] S. Zhu, R.H. Pelton, K. Collver, Mechanistic modelling of fluid permeation through compressible fiber beds, Chem. Eng. Sci. 50 (22) (1995) 3557–3572.

[32] J. Newman, K.E. Thomas-Alyea, Electrochemical Systems, John Wiley & Sons, 2012.

[33] A.A. Shah, M.J. Watt-Smith, F.C. Walsh, A dynamic performance model for redox-flow batteries involving soluble species, Electrochim. Acta 53 (27) (2008) 8087–8100.

[34] D. Schmal, J. Van Erkel, P.J. Van Duin, Mass transfer at carbon fibre electrodes, J. Appl. Electrochem. 16 (3) (1986) 422–430.

[35] J.T. Gostick, M.W. Fowler, M.D. Pritzker, M.A. Ioannidis, L.M. Behra, In-plane and through-plane gas permeability of carbon fiber electrode backing layers, J. Power Sources 162 (1) (2006) 228–238.

[36] E. Sum, M. Skyllas-Kazacos, A study of the V (II)/V (III) redox couple for redox flow cell applications, J. Power Sources 15 (2–3) (1985) 179–190.

[37] T. Yamamura, N. Watanabe, T. Yano, Y. Shiokawa, Electron-transfer kinetics of Np3+/ Np4+, NpO2+/ NpO2 2+, V2+/ V3+, and VO2+/ VO2+ at carbon electrodes, J. Electrochem. Soc. 152 (4) (2005) A830.

[38] M. Pourbaix, Atlas of electrochemical equilibria in aqueous solution, NACE (1974) 307.

[39] D. You, H. Zhang, J. Chen, A simple model for the vanadium redox battery, Electrochim. Acta 54 (27) (2009) 6827–6836.

[40] J. Sun, H. Jiang, C. Zhao, X. Fan, C. Chao, T. Zhao, Holey aligned electrodes through in-situ ZIF-8-assisted-etching for high-performance aqueous redox flow batteries, Sci. Bull. 66 (9) (2021) 904–913.

Qijiao He received her B.Eng. (2015) and M.Eng. (2019) degrees from Northwestern Polytechnical University. She is currently a Ph.D. student in Prof. Meng Ni's group at the Hong Kong Polytechnic University. Her research mainly focuses on the solid oxide fuel cells and redox flow batteries.

Jie Yu completed her PhD program in Chemical Engineering from Nanjing Tech University, P. R. China, in 2018. She is now a postdoctoral fellow in Hong Kong Polytechnic University, Hong Kong, China. Her research interests focus on design and synthesis of perovskite oxides, metal sulfides, metal phosphides, and carbon composites and their applications in electrochemical catalytic fields.

Zixiao Guo received his B.Eng. degree from Zhejiang University in 2019. Now he is a Ph.D. student in Prof. Tianshou Zhao's group at the Department of Mechanical and Aerospace Engineering of Hong Kong University of Science and Technology. His research mainly focuses on the multi-scale simulation on energy storage.

Jing Sun obtained her B.E. (2014) and M.Eng. (2017) degrees from University of Science and Technology Beijing, and Ph.D. (2021) from Hong Kong University of Science and Technology. She is currently a visiting scholar at the Department of Mechanical and Aerospace Engineering of Hong Kong University of Science and Technology. Her research mainly focuses on the electrode material design in redox flow batteries.

Siyuan Zhao received his B.Eng. degree in Vehicle Engineering from Beijing Institute of Technology in 2020. Now he is a Ph.D. student at the Hong Kong Polytechnic University. His research interests focus on metalair batteries and zinc-based batteries.

Professor Tianshou Zhao is a Chair Professor at Hong Kong University of Science and Technology. He has made seminal contributions in the areas of fuel cells, advanced batteries, multi-scale multiphase heat and mass transport with electrochemical reactions, and computational modeling. In addition to 4 edited books, 9 book chapters and over 70 keynote lectures at international conferences, he has published 330 papers in various prestigious Journals. Prof Zhao has in recent years received many awards, examples include: 2014 Distinguished Research Excellence Award (HKUST), State Natural Science Awards (2012, 2013), The Ho Leung Ho Lee Prize for Scientific and Technological Advancement, Croucher Senior Fellowship award, 2018 Science Bulletin Best Paper Award, Overseas Distinguished Young Scholars Award (NSFC), Yangtze River Chair Professorship, among others. In the international community, Prof Zhao serves as: Editor-in-Chief, International Journal of Heat and Mass Transfer (Elsevier) 2019- Editor-in-Chief, Applied Thermal Engineering (Elsevier) 2003-2019; Member of Advisory Board, Energy & Environment Science (RSC) 2008.

Prof. Meng Ni is a Professor and Associate Dean (Research) at The Hong Kong Polytechnic University. He is Humboldt Fellow (Germany). Prof. Ni's research includes high temperature fuel cells, Zn-air batteries, flow batteries, and electrochemical system for low grade heat utilization. He is a Senior Editor of *Sustainable Energy Technologies and Assessments* (Elsevier), e-Prime- Advances in Electrical Engineering, Electronics and Energy (Elsevier), and an Associate Editor of International Journal of Energy Research (Wiley) and International Journal of Green Energy (Taylor and Francis).